CHEMISTRY OF MATERIALS

pubs.acs.org/cm Article

Impact on the Formation and Catalytic Property of Pt-Based Nanocatalysts by Galvanic Reaction with Co-Reduction Agents

John R. Crockett, Maggie Wang, Joseph E. Doebler, Tejal Pawale, Xiao Li, and Ying Bao*

Cite This: *Chem. Mater.* 2022, 34, 9282−9293 Read Online

ACCESS | Metrics & More | Article Recommendations | Supporting Information

ABSTRACT: It has been shown that controlling the morphology and composition of Pt-based nanocrystals can effectively enhance catalytic properties. We report a detailed study on the impact of using co-reducing agents in the galvanic replacement reaction (GRR) between Ag shell templates and Pt precursors to better control the morphology, composition, and resulting performance of the fabricated Pt-based catalysts. Mesoporous silica-supported silver shell-coated gold nanodumbbell nanostructures (AuNDB@Ag@mSiO_2) are synthesized via reducing silver ions which have penetrated through the mSiO_2 layer and then be deposited on the surface of the AuNDBs. These are used as templates and the morphology and optical properties of these templates can be adjusted by altering the amount of Ag^+ in the depositing condition. The mSiO_2 layer shows some flexibility and does not influence the silver shell formation on the surface of AuNDBs. Additionally, the thickness of the silver shell of the template and the strength of the reducing agent used in the GRR impact the morphology, composition, and catalysis performance of the resulting Pt-based catalysts. A plausible mechanism on those observations is studied and discussed.

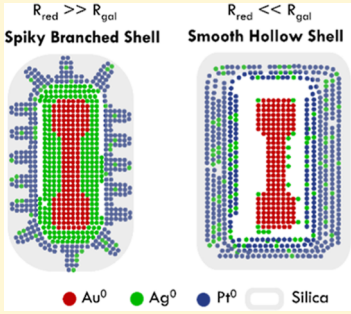

Downloaded via WESTERN WASHINGTON UNIV on October 25, 2022 at 15:58:28 (UTC).
See https://pubs.acs.org/sharingguidelines for options on how to legitimately share published articles.

■ INTRODUCTION

Platinum (Pt)-based materials have been extensively used as catalysts in a wide range of reactions, including catalytic conversion,[1] hydrogenation, oxidation,[2] and reduction.[3,4] However, Pt is expensive and has limited reserves, resulting in drawbacks of utilizing Pt for various applications. Thus, a wide range of many experimental and theoretical studies have been motivated by developing approaches to maximize Pt's catalytic performance.

In general, increasing the surface area of Pt as well as integration with other metals (e.g., Pd, Au, Ag, Fe, and Cu) to form alloyed or multiple-component metallic nanomaterials are two effective approaches to improve Pt's catalytic performance. For example, the Nørskov group used density functional theory to study various aspects of Pt-based metal clusters on oxygen reduction reactions for fuel cells.[5] Adzic group and Stamenkovic group reported many studies of Pt or Pt-bimetallic monolayers or multilayers on supported substrates for fuel cells, and their experimental results are often supported by computational work from the Mavrikakis group.[6−8] Pt or Pt alloy metal clusters deposited on film or other supported surfaces have also been studied by Brankovic, Shao, M., and Dimitrov groups.[9−13] Although systems including synthesizing freestanding small-sized nanoclusters or depositing metal atoms on the substrate have shown significant progress, they have their own drawbacks, such as tending to sinter (form bigger particles) or dissolving due to their small particle instability as well as detaching from their supporting surface.[14−17]

An alternative system that focuses on fabricating self-stabilized Pt-based colloidal nanoparticles has also received a lot of attention. So far, significant progress has been made in the colloidal nanoparticle system toward this goal, though key challenges remain. One approach to enhance Pt's catalytic performance has focused on synthesizing Pt nanostructures with controlled morphologies.[18,19] El-Sayed and co-workers demonstrated that the shape of platinum nanoparticles affected their catalytic activity toward the reduction of hexacyanoferrate.[20] Their study demonstrated that there was a direct relationship between the percentage of available edge or corner sites and the catalyst activity among various shapes of Pt resulting in the highest activity with the tetrahedral catalysts (the most edge and corner sites). More generally, hollow structures, porous structures, and dendrite structures have large specific surface areas and enormous active sites.[21−23] A second approach to improve Pt's performance for various electrocatalytic reactions has been to introduce other metals (e.g., Au, Ag, Fe, and Cu) to Pt and form alloyed or multiple-component metallic nanomaterials.[24−26] Pt-based heterogeneous metallic nanocrystals have shown enhanced catalytic properties in comparison with pure Pt nanocrystals due to a strong electronic coupling between the metals.[27]

Combining these two approaches by developing methods to synthesize Pt-based multi-metallic nanocrystals with a large

Received: August 29, 2022
Revised: September 29, 2022
Published: October 12, 2022

ACS Publications © 2022 American Chemical Society

https://doi.org/10.1021/acs.chemmater.2c02659
Chem. Mater. 2022, 34, 9282−9293

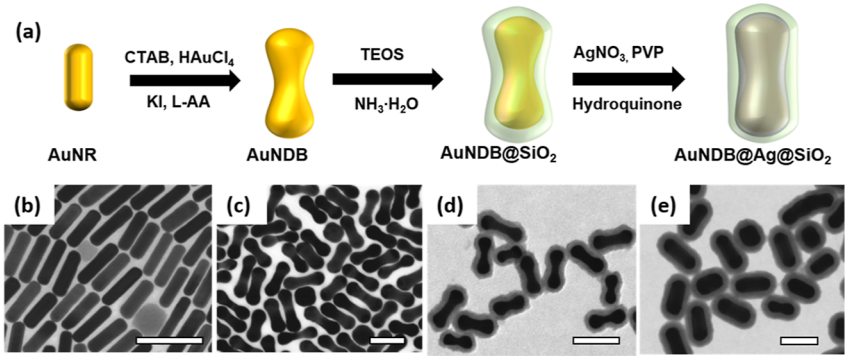

Figure 1. (a) Illustration of the synthesis of a mesoporous silica shell-supported AuNDB@Ag nanostructure. (b−e) STEM images of (b) AuNRs, (c) AuNDBs, (d) AuNDB@silica (AuNDB@mSiO_2), and (e) silver-deposited AuNDB@silica (AuNDB@Ag@mSiO_2). Scale bar: 100 nm.

surface area is a promising direction for additional improvements in catalytic performance, as discussed in a number of studies.[28,29] Strategies to obtain a high surface area of Pt such as sequential reduction of platinum on top of a particle template with large surface area or reduction of platinum on top of a particle with post treatment are effective.[30,31]

However, galvanic replacement reaction (GRR) has emerged as one of the most popular synthesis method.[32−35] It offers a unique advantage in that it can create platinum-based multi-metallic nanostructures whose shape,[35] size,[35] and composition[36] can be precisely controlled without the need for post-synthetic modifications (annealing) or an applied potential. Hollow Pt−Ag nanocatalysts, obtained via simple GRR between a Pt precursor and sacrificial Ag templates, have been commonly synthesized and were pioneered by the Xia group.[37−40] Their recent study has also demonstrated that Pt/Ag nanocatalysts have great catalytic performance for oxygen reduction reactions.[37]

The GRR can be coupled with co-reduction by introducing a reductant into the GRR. With the addition of the secondary reducing agent, the shape and composition of the resulting nanostructure can be manipulated beyond what can be achieved in the simple galvanic replacement as the secondary reducing agent introduces new pathways and products to the reaction. To fabricate the desired nanostructure, one must carefully control both the rates of co-reduction and GRR. For example, the Xia group has successfully synthesized Pd−Pt nanocages with greatly enhanced catalytic activities by coupling the GRR between Pd nanocubes and K_2PtCl_4 with a co-reduction process by using citric acid as the reductant.[41] Although Xia groups' nanostructures have displayed excellent catalytic properties, Pd is another expensive metal in the platinum family. Thus, using Pt and a relatively cheaper metal for the GRR would be beneficial, and silver has been frequently preferred because of its very low redox potential.[42−44] However, there are only a few reports demonstrating the use of both Ag templates/Pt precursors and co-reduction in a GRR to generate Pt-based nanostructures.[45,46] Camargo group studied the different impacts on the morphology of synthesized AgPt nanomaterial when performing GRR with and without a co-reduction agent.[45,46] To the best of our knowledge, there are no reports studying in detail on the impact of reduction agents on fabricating Pt-based nanocatalysts via the galvanic replacement approach with the Ag template. Additionally, there is a lack of understanding on the effect of the catalytic performance due to the resulting morphology and composition of the nanostructures.

In this paper, Pt-based catalysts are obtained using GRR coupled with co-reducing agents between Ag shell templates and Pt precursors. The Ag shell template is created by first synthesizing a mesoporous silica (mSiO_2) shell-supported gold nanodumbbell (AuNDB) nanostructure, where the mSiO_2 stabilizes the nanostructure for further treatment. Due to the porosity of the mSiO_2 shell, silver ions will penetrate the shell and deposit on the surface, forming the AuNDB@Ag@mSiO_2 template for GRR. The morphology of this template (specifically the thickness of the silver shell) will also be able to be adjusted by altering the amount of Ag^+ used. With the fabricated AuNDB@Ag@mSiO_2 nanostructures, hydroquinone (HQ) and AA will be separately used as reducing agents to assist the GRR between the Pt precursor and Ag sacrificial template. Varying the thickness of the silver shell and the strength of the reducing agents will impact the rates of co-reduction and GRR in the system and will affect the final morphology and composition of the Pt-based catalysts. The mechanism of catalyst formation is proposed and supported with evidence from further characterization. The catalytic performance of the resulting Pt-based catalysts was evaluated in the reduction reaction of 4-nitrophenol (4-NP) to 4-aminophenol. The relationship between the morphology and composition of nanostructures and their catalytic performance, as well as the proposed mechanism behind this, are discussed.

■ RESULTS AND DISCUSSION

Creation of AuNDB@Ag@mSiO_2 Nanostructures for Use as GRR Template. Following the process illustrated in Figure 1a, mesoporous silica shell-supported AuNDB@Ag nanostructures (AuNDB@Ag@mSiO_2) were created for later use as templates in a GRR withPt^{2+}. The synthesized products from each step in this process were characterized via scanning transmission electron microscopy (STEM) and representative results are shown in Figure 1b−e. Initially, gold nanorods (AuNRs) with an aspect ratio of 3.8 ± 0.6 were synthesized using a previously published method, with representative results shown in Figure 1b.[47,48] Next, AuNDBs were formed based on an iodide-mediated growth using synthesized AuNRs as seeds, and the formation mechanism is discussed in more detail in the Supporting Information.[49] Compared to the AuNR seeds, the resulting AuNDBs have an increased aspect ratio 5 ± 2, which can be observed in Figure 1c, a representative STEM image of AuNDBs. It is worthwhile to mention that the samples are not 100% AuNR and AuNDBs; there are some byproducts such as spheres resulting from the synthesis process. AuNDBs were then coated with a

https://doi.org/10.1021/acs.chemmater.2c02659
Chem. Mater. 2022, 34, 9282−9293

mesoporous silica shell (AuNDB@$mSiO_2$), as discussed in detail in the Experimental Section. Figure 1d shows a representative STEM image of the resulting nanoparticles and the formed $mSiO_2$ shells with thickness of approximately 19 nm, measured on either side of the AuNDBs. A layer of silver shell was deposited via the reduction of $AgNO_3$ onto the surface of the AuNDBs to form AuNDB@Ag@$mSiO_2$, which altered the shape of the nanostructures from dumbbell-like back to a rod-like shape, representative results of which are shown in Figure 1e. Note that the exact shape will depend on the amount of $AgNO_3$ added, which will be discussed in more detail later. This indicates that the silver ions can penetrate through the silica shell due to its porosity and be reduced on the Au surface. In addition, this demonstrates that the $mSiO_2$ shell is flexible to some extent, because the previously dumbbell shaped shell changed to a rod-like shape due to enlargement of the core particle. The optical properties of the products were also monitored at each step. The results, alonge with a detailed discussion, are shown in Figure S1.

The synthesized AuNDB@Ag@$mSiO_2$ was further studied to better understand the silver deposition process on AuNDB@$mSiO_2$. Figure 2a is the STEM image obtained by combining bright field and high-angle annular dark-field (HAADF), demonstrating the details of the nanostructures. The light areas on the image are the silica shells, while the darkest areas are the AuNDBs. The Ag overgrowth appears as lighter gray thin layers surrounding the AuNDBs. This shows that the silver layer is thicker in the center of the dumbbell structure, while it becomes thinner toward the rod tips. To further confirm the deposition sites of the Ag atoms on AuNDB@Ag@$mSiO_2$, HAADF-STEM and energy-dispersive X-ray spectroscopy (EDX) were performed to examine the spatial distribution of Ag and Au on a single nanostructure (Figure 2b). The HAADF-STEM image is shown in the first panel of Figure 2b. Because the HAADF-STEM image is formed by collecting the scattered electrons, silica does not appear in the image due to its low atomic number and weak electron interaction, while gold and silver appear bright in the image due to their higher atomic number and stronger electron scattering. The corresponding elemental mappings (second and third panel of Figure 2b) clearly show the presence of Ag as a shell surrounding the Au atoms. The map of Ag atoms show less silver on the tips of the rod structures, while most Ag atoms are located on the center of the dumbbell structure, which agrees with STEM results in Figure 2a. The preferential silver reduction at the central area of the AuNDBs or Au NRs instead of the tips has also been observed by others in a similar deposition process that did not involve a silica shell.[50,51] It is known that silver overgrowth takes place preferentially at the high-energy facets, including <100> and <110>, which tends to reduce the free surface energy.[52,53] Because the <100> and <110> are richly located on the lateral side, not on the tip of AuNDBs or Au NRs, silver deposition preferentially takes place on its lateral facets.[51]

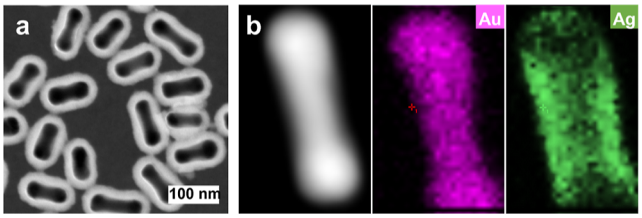

Figure 2. (a) STEM image of AuNDB@Ag@$mSiO_2$, (b) HAADF-STEM, and elemental mapping of one AuNDB@Ag@$mSiO_2$. The pink and green colors in the elemental maps stand for gold (Au) and silver (Ag), respectively.

Figure 3 depicts representative STEM images of AuNDB@Ag@$mSiO_2$ nanostructures when varying volumes of $AgNO_3$

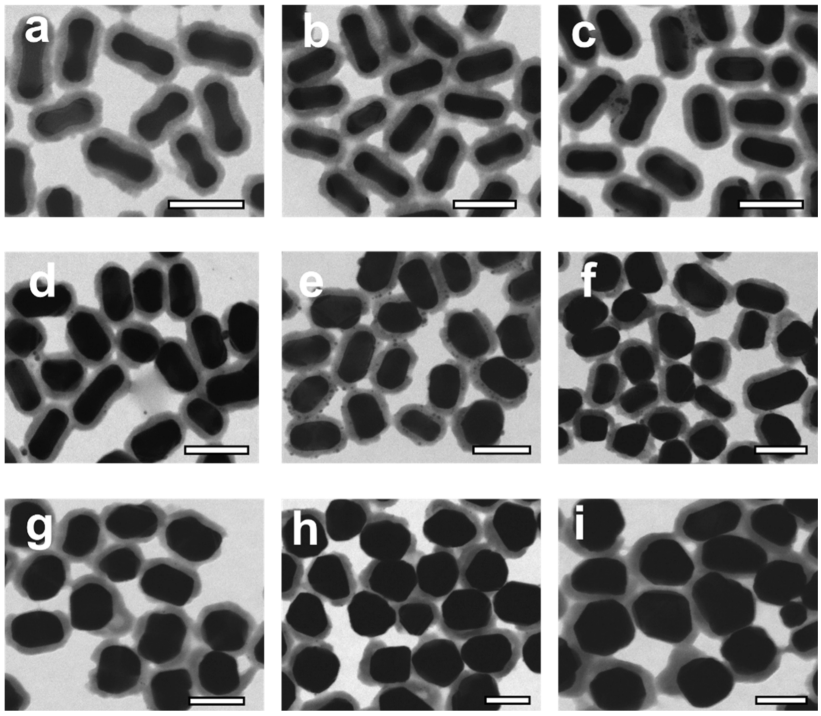

Figure 3. STEM image of AuNDB@Ag@$mSiO_2$ with varying volume fractions of silver obtained by adding different amounts of a 10 mM silver nitrate solution: (a) 10, (b) 20, (c) 30, (d) 40, (e) 50, (f) 60, (g) 100, (h) 120, and (i) 200 μL. Scale bar: 100 nm.

https://doi.org/10.1021/acs.chemmater.2c02659
Chem. Mater. 2022, 34, 9282−9293

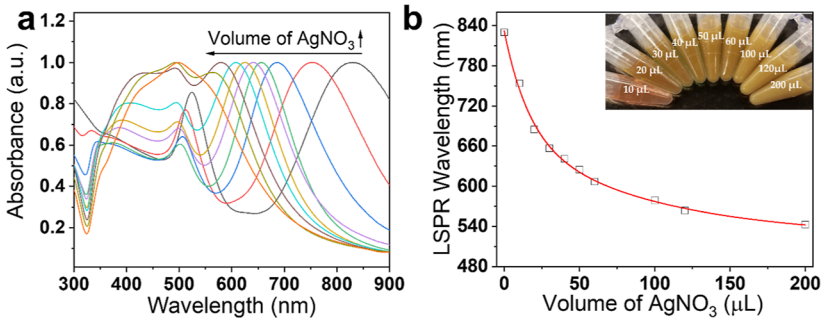

Figure 4. (a) UV−vis absorption spectra of AuNDB@Ag@mSiO$_2$ nanostructures with varying volume fractions of silver obtained by adding different amounts of a 10 mM silver nitrate solution: (from right to left spectra) 0, 10, 20, 30, 40, 50, 60, 100, 120, and 200 μL, respectively. (b) LSPR peak location as a function of silver nitrate solution volume; (insert) color changes as the silver nitrate volume increases.

were used in the Ag deposition process. The morphology of the AuNDB@Ag@mSiO$_2$ changes with increased Ag^+ ion concentration in the growth solution. At the lowest volume of $AgNO_3$ (10 μL, shown in Figure 3a), the Ag shell seems quite thin and the Ag mainly reduced at the central area of the AuNDBs, keeping the silica shell in a dumbbell-like shape. As volume increases to 20, 30, and 40 μL, the Ag shell becomes thicker, and the enlarged Ag shell pushes the encompassing silica shell outward, taking on a cylindrical rod shape (shown in Figure 3b−d). When the volume of $AgNO_3$ increases further from 50 to 200 μL, an anisotropic Ag coating occurs, which results in increased width of the nanoparticle and an irregularly shaped AuNDB@Ag. This anisotropic growth process is consistent with previously reported silver deposition on silica shell-free AuNRs, indicating that the mSiO$_2$ shell did not influence the NP growth behavior.[54] In addition, we can observe in Figure 3d−i that the mSiO$_2$ shell becomes thinner and eventually breaks under high volumes of silver deposition, which is the result of the pressure from the enlarged NPs. This result clearly demonstrates that the mSiO$_2$ shell is not rigid; instead, it is elastic to some extent. The mSiO$_2$ allows the growth of AuNDB@Ag while still supporting the stability of enlarged nanostructure in solution. The elastic characterization of the mSiO$_2$ shell at extremely thin thickness will be of great interest to explore the reversibility and adaptability of the irregularly shaped mSiO$_2$ shell in our future work, which is beyond the scope of this current work.

Optical properties of the nanoparticles can be also tailored by forming silver shells of varied thickness on the surface of the AuNDBs. The AuNDB@mSiO$_2$ without silver coating (0 μL of $AgNO_3$) has a LSPR peak located at 830 nm. With progressively increased volume, it is clearly observed from Figure 4a that the LSPR peak undergoes a continuous blue shift. Eventually, with 200 μL of $AgNO_3$, the LSPR is merged with other peaks, forming a broad peak which is understandable as the silver content is very high, and causing the nanostructure to take an irregular sphere shape. The peak positions of all the samples have been fitted and found to obey the exponential decay behavior, as shown in Figure 4b. Note: the LSPR peak position from the 200 μL sample is estimated because it is not a distinguishable separated peak. It is necessary to mention that the additional silver deposition is crucial in observing a wide shift in the LSPR peak position. The corresponding photo of nanoparticle solution in the inset of Figure 4b demonstrates the effect of increased silver content on the solution color. Moving from low to high silver content, the solution color changes from light red to muddy orange.

Reducing Agent-Assisted Galvanic Replacement for the Formation of Pt-Based Nanocatalysts. The Ag shell of the silica shell-supported AuNDB@Ag nanostructure created in the prior section is used as a sacrificial template to guide the formation of Pt via the GRR between the Ag shell template and the Pt precursor. During the GRR, the reducing agents, HQ and ascorbic acid (AA), are used and their impact on the morphology is studied.

Transmission electron microscopy (TEM) image (Figure 5a) shows the detailed morphology of the nanomaterial

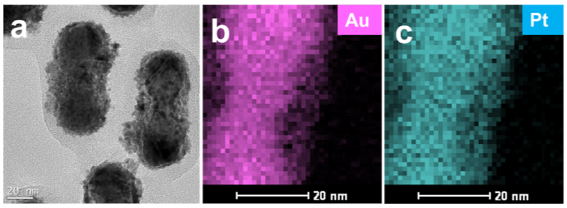

Figure 5. (a) TEM image of a HQ-assisted Pt-based nanocatalyst using AuNDB@Ag@mSiO$_2$ made with 20 μL of $AgNO_3$ (Ag/Pt = 2/2), (b,c) elemental mapping of one galvanic reacted metal nanostructure. The pink and blue colors in the elemental maps stand for Au and Pt, respectively. Ag result omitted due to non-detection.

obtained by using HQ as a co-reducing agent and K_2PtCl_4 as a Pt precursor to react with AuNDB@Ag@mSiO$_2$ nanostructures made with 20 μL of $AgNO_3$. The resulting nanocatalysts maintained a full silica shell coating. The metal nanostructure retained a dumbbell shape for its core but the shell became a hollow structure with a rough surface instead of a uniform silver layer. EDX was performed to examine the spatial distribution of the metal elements on a single nanostructure, and the results are shown in Figure 5b,c. The Au element distribution shows that the AuNDB still maintains the dumbbell shape. The hollow structure appears to have Pt elements. Ag was not able to be detected and this result is omitted from Figure 5. This indicates that the Ag shell is fully replaced by Pt via the co-reduction GRR. The UV−vis spectra of nanostructure before and after the galvanic reaction are shown in Figure S2. From the spectra, it can be noted that the silver peak at 340 nm (indicated with red dashed circle) is barely recognizable after the galvanic reaction which supports the EDX results. Additionally, the LSPR has a red-shift to 820 nm which is closer to the LSPR of AuNDB@Ag@mSiO$_2$ nanostructures (830 nm), indicating the absence of the plasmon coupling effect from the Ag shell.

https://doi.org/10.1021/acs.chemmater.2c02659
Chem. Mater. 2022, 34, 9282−9293

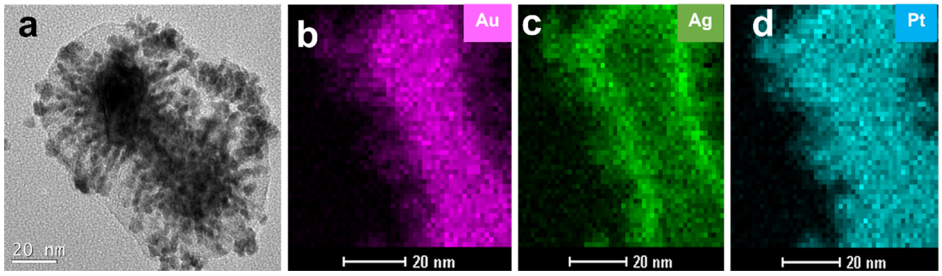

Figure 6. (a) TEM image of AA-assisted Pt-based nanocatalyst using AuNDB@Ag@mSiO$_2$ made with 20 μL of AgNO$_3$ (Ag/Pt = 2/2), (b−d) elemental mapping of one galvanic reacted metal nanostructure. The pink, green, and blue colors in the elemental maps stand for Au, Ag, and Pt, respectively.

The same HQ-assisted galvanic reaction was performed with all the AuNDB@Ag@mSiO$_2$ made with different amounts of silver content, as discussed in the previous section. The calculated Ag/Pt molar ratios for all the AuNDB@Ag@mSiO$_2$ are $x/2$, where x = 1, 2, 3, 4, 5, 6, 10, 12, and 20. Throughout this paper, Ag and Pt concentrations will be described as molar ratios between Ag and Pt; their GRR is as follows: $PtCl_4^{2-} + 2Ag \rightarrow Pt + 2Ag^+ + 4Cl^-$, which shows that in order to replace all the Ag present without a co-reducing agent, it requires a Pt/Ag ratio of 1/2. It also indicates that samples with a Ag/Pt molar ratio more than 4/2 will not be fully galvanically reacted in the absence of a co-reducing agent.

Representative STEM images of resulting nanostructures with various Ag/Pt molar ratios are shown in Figure S3a−i. Note the amount of Pt remains constant and only the Ag content is changing. With the lowest molar ratio (Ag/Pt = 1/2), it can be observed that the hollow shell structure is present with tiny gaps between the shell and the AuNDB core. In addition, there are numerous spiky features on the hollow structure. These spiky structures fade away as the molar ratio increases. The space between the core and hollow shell is increased with increasing molar ratio. This is reasonable because the silver shell thickness increases with increased molar ratio. During the galvanic reaction, the silver shell is the template metal which will be oxidized and dissolved in solution while Pt, the oxidant metal, will be reduced onto the surface of the particle. Thus, the larger the particle is, the larger the volume of the shell will be.

Due to the observation of numerous spiky features on the hollow structure that formed from the lowest molar ratio (Ag/Pt = 1/2) by HQ co-reduction, a stronger reducing agent, AA, was selected to study the impact on the morphology formation of Pt-based nanocatalysts via a stronger reducing agent-assisted galvanic reaction. Initially, the galvanic reaction was carried out on AuNDB@Ag@mSiO$_2$ nanostructures made with 20 μL of AgNO$_3$. The UV−vis spectra (Figure S4) after the reaction are dramatically different from the one obtained before the reaction. The absorbance intensity is increased from the 0.2−1.0 range to the 1.0−1.5 range. Previously there were two large peaks, but after the reaction, these were no longer able to be identified and leaving only a small peak around 530 nm. This is also different from the sample obtained when using HQ reducing agent, as discussed earlier. The TEM image (Figure 6a) shows that the morphology of the synthesized sample using AA is significantly different from the one using HQ. The fabricated nanostructure does not show a clear hollow structure. Instead, there are a great number of spiky branches. It has been reported that the spiky branched features often results from kinetic control synthesis conditions, where the reaction rate is slower than the normal reaction, and the reduced atoms migrate to the surface of metal to form the spiky branches under the guidance of a "diffusion-limited aggregation" strategy.[23,55] In our work, the kinetic control condition is formed by using relatively weak reducing agents (HQ and AA), the metal ions are reduced in solution and slowly migrate back to form the spiky branches. We believe that the mesoporous silica shell possibly affects how the metal atoms are transported to the deposition locations and form the unique spiky branches. The impact of silica shell for the kinetic controlled deposition process will be studied in the future.

The EDX results in Figure 6b−d show that the Au element distribution exhibits the dumbbell shape. The silver element was distributed mostly on the shell surrounding the AuNDB, though it also has relatively high atom intensity on the spiky branches, indicating that the formed branches are partly made of silver. The platinum element distributed across the whole nanostructure and the overall shape closely matches a combination of gold plus silver element distributions. It is worthwhile to mention that the spiky feature with a relatively weak intensity in the Au element map (Figure 6b) is an artifact due to the EDX peak overlap between Au and Pt. From this result, we believe that platinum is not only on the surface of nanostructure after the galvanic reaction but also mixed with silver. The high-resolution TEM (HRTEM) helps to reveal the crystal information of the surface of nanostructure and further our understanding on the Pt and Ag formation, as shown in Figure S5. The measured lattice spacings (Figure S5b) are ∼0.23 nm which is larger than that of Pt(111) (0.226 nm) and smaller than that of Ag (111) (0.236 nm), implying the generation of a Pt−Ag alloy.[56,57] To further support the formation of the AgPt alloy, we performed X-ray photoelectron spectroscopy (XPS) measurement on the sample (Ag/Pt molar ratio = 3/2) prepared by an AA-assisted GRR to analyze the surface chemical composition. As shown in Figure S6, the peaks of Ag 3d5/2 and Ag 3d3/2 located at 367.38 and 373.21 eV indicate that the metallic state Ag^0 is absolutely predominant in the composite. Meanwhile, there are two peaks at binding energies of 313.88 and 331.08 eV resulting from Pt 4d5/2 and 4d3/2 for the composites. A noticeable shift of the Pt 4d5/2 and 4d3/2 binding energy relative to that of pure Pt (315 eV for Pt 4d5/2 and 330 eV for Pt 4d3/2 indicated by green dash line) is probably due to the electron donation from Ag to Pt in the formation of AgPt alloy. Similar peak shifts of Pt energy peaks in AgPt alloy have been observed and reported from other works.[58,59]

The same AA-assisted GRR was performed with all the AuNDB@Ag@mSiO$_2$ made with different amounts of silver content, including the Ag/Pt molar ratios $x/2$, where x = 1, 2,

https://doi.org/10.1021/acs.chemmater.2c02659
Chem. Mater. 2022, 34, 9282−9293

3, 4, 5, 6, 10, 12, and 20. Representative STEM images of the resulting nanostructures with various Ag/Pt molar ratios are shown in Figure S7a-i. They reveal that with low molar ratio Ag/Pt = 1/2, 2/2, 3/2, and 4/2, the nanostructures not only have prominent spiky branches but also the hollow shell structures are less obvious and uniform on individual nanoparticles. With the increased molar ratios, the spiky branches slowly fade out and the hollow shell becomes clear and larger with increased silver shell thickness.

Mechanism of Catalyst Formation Using Reducing Agents. Here, we propose a plausible mechanism that can account for the morphology changes under certain reducing agents and various Ag/Pt molar ratios. This mechanism should account for key results observed in our data and we review those in one place here. For the HQ system, (1) the nanocatalyst fabricated with molar ratio Ag/Pt = 2/2 shows Au and Pt elements but Ag is undetectable; (2) the hollow shell formation is clearly observed within all the nanocatalyst samples; and (3) the nanocatalyst fabricated with the lowest molar ratio (1/2) appears to have fuzzy spikes on the surface of the shell. However, as the molar ratio is increased, the fuzzy spikes quickly fade out—for example, it is difficult to observe them even in the sample fabricated with a molar ratio of 2/2. In addition, the shell volume increases with increased molar ratio. For the AA system, (1) the nanocatalyst fabricated with molar ratio Ag/Pt = 2/2 shows Au, Ag, and Pt elements and the HRTEM indicates that the Ag−Pt forms an alloy on the surface of the nanostructure; (2) the hollow shell structures are less obvious for low molar ratio samples such as Ag/Pt = 1/2, 2/2, and 3/2; and (3) the nanocatalyst fabricated with relatively low molar ratio (1/2, 2/2, 3/2, and 4/2) appears to have spiky branches on the surface of the shell and with higher molar ratios they slowly disappeared. In addition, the shell volume increases with increased molar ratio.

There are four possible reactions involved in the process. (1) The galvanic replacement between Ag and $PtCl_4^{2-}$ (reaction: $PtCl_4^{2-} + 2Ag \rightarrow Pt + 2Ag^+ + 4Cl^-$); (2) the reduction of $PtCl_4^{2-}$ by a reducing agent (reaction: $PtCl_4^{2-}$ + reducing agent → Pt + $4Cl^-$); (3) the reduction of produced Ag^+ by a reducing agent (reaction: Ag^+ + reducing agent → Ag); and (4) the formation of AgCl precipitate if the concentrations of Ag^+ and Cl^- are high enough (reaction: $Ag^+ + Cl^- \rightarrow AgCl$). The galvanic reaction, reaction (1), will lead to the formation of a hollow structure,[43,60,61] whereas the reduction by a reducing agent will result in the formation of a spiky branch shell on the AuNDB@Ag@mSiO_2 nanostructure mainly due to the kinetic controlled deposition process. Reactions (2) and (3), the reductions by the reducing agent, compete with reaction (1), the galvanic replacement.

The standard redox potential of $PtCl_4^{2-}$/Pt (+0.76 V) is lower than that of Ag^+/Ag (+0.8 V) which allows the galvanic reaction to occur. For the reducing agents, the redox potential for HQ is E° = 0.7 V, and for AA is E° = 0.35 V.[62,63] The more positive the potential is, the greater the species' affinity for electrons and the more the species tends to be reduced. From this, we know that the AA has more positive potential, which means a stronger reducing ability, in terms of reducing $PtCl_4^{2-}$ to Pt and Ag^+ to Ag than HQ has. From the redox potential values of the key species and the observed previous results, we infer that the HQ has weak or no reducing capability in this context, which results in weak or no parallel reduction by HQ when competing with the galvanic reaction. In contrast, the AA has a strong reducing power which can be clearly observed due to the Ag/Pt alloy spiky branch formation previously discussed. The reaction rates of the competing reactions can be controlled by the concentration of AA and Ag. In our case, the reaction pathway is controlled by keeping the reduction rate (R_{red}) constant and manipulating the galvanic rate (R_{gal}) by varying the silver shell thickness and hence the obtained morphology of the final product. When the silver shell is relatively thin, the reducing reaction will dominate while the galvanic reaction barely takes place. In this case, part of the $PtCl_4^{2-}$ is reduced by the reducing agent into a Pt atom and epitaxially deposits on the surface of the Ag nanoparticle to form the incomplete thin Pt shell. Meanwhile, $PtCl_4^{2-}$ can oxidize a small part of the Ag shell through galvanic replacement. The Ag^+ produced by the galvanic replacement can also be reduced by AA and then deposit on the newly formed Pt layer, forming a porous Ag−Pt alloy shell. Due to the porous structure of the silica shell, the Ag−Pt alloy structure becomes spiky branches as illustrated in Figure 7 (top panel) and the experimental results in Figure S7a. In the case of a thick silver shell, the GRR would be faster than the reduction reaction of AA. As a result, the inner Ag shells are totally removed by galvanic replacement and the hollow porous Pt shells are built as illustrated in Figure 7 (bottom panel) and the experimental results in Figure S7i.

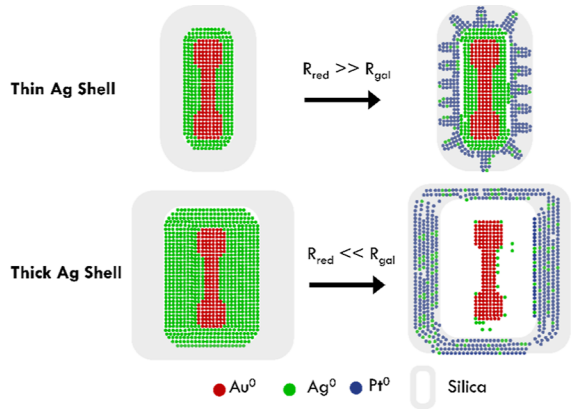

Figure 7. Schematic illustration of the two possible routes and products for synthesis that involve aAg shell and Pt precursor in the presence of thin and thick silver shells under the AA-assisted GRR system.

The R_{gal} can be investigated by recording the UV−vis spectra during the reaction at different times. In this case, the UV−vis spectra during the reaction on samples with molar ratio of Ag/Pt = 3/2 and 5/2 were recorded separately over 15 min intervals, as shown in Figure S8a and b. From the spectra, it is clear that the sample with Ag/Pt molar ratio = 3/2 has substantially more separated spectra than the sample with Ag/Pt molar ratio = 5/2, which indicates that the reaction on the sample with Ag/Pt molar ratio = 3/2 takes longer to complete as compared to the reaction in the sample with Ag/Pt molar ratio = 5/2. In addition, during the reaction process, the peak initially located at 510 nm shows a gradual shift in both wavelength and intensity and eventually does not change further, which indicates that the reaction is complete. The intensity value of this peak was then analyzed and plotted as a function of reaction time, as shown in Figure S8c. It is very clear that the sample with Ag/Pt molar ratio = 5/2 takes a much shorter time to reach the maximum intensity and to

https://doi.org/10.1021/acs.chemmater.2c02659
Chem. Mater. 2022, 34, 9282−9293

complete the reaction. This is evidence that the R_{gal} will increase with increased Ag/Pt molar ratios, which in this context means thicker silver shells.

To support the hypothesis that the Ag^+ ions were reduced by AA, one item of evidence is that with a higher molar ratio, there are no AgCl crystals observed. The representative scanning electron microscopy (SEM) image (Figure 8a) of

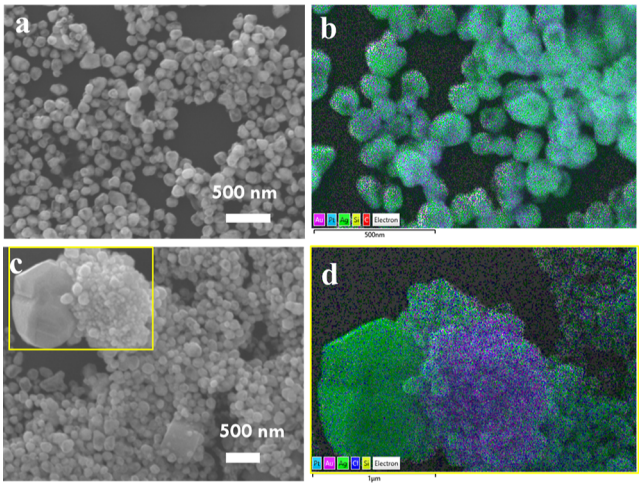

Figure 8. (a) SEM image of the sample with the highest molar ratio (Ag/Pt = 20/2) prepared under AA-assisted GRR; (b) EDX mapping layered image of the sample in (a); (c) SEM image of the sample with the highest molar ratio (Ag/Pt = 20/2) prepared under HQ-assisted GRR; and (d) EDX mapping layered image of sample in (c) roughly at highlight yellow box.

the sample with the highest molar ratio (Ag/Pt = 20/2) shows that no big crystal appears. Under EDX, there are no Cl elements that can be detected, as shown in Figures 8b and S9a. To confirm that AA also reduced $PtCl_4^{2-}$ to Pt, all samples were studied by EDX and the atomic ratio of Ag/Pt was plotted against the volume of silver nitrate in Figure S10. Reaction (1) shows that to complete the galvanic replacement, the Ag/Pt molar ratio must be at least 4/2. This indicates that a Ag/Pt molar ratio less than 4/2, such as 1/2, 2/2, or 3/2, will not have a complete galvanic replacement. If that is the case, there should have been excess $PtCl_4^{2-}$ in solution. However, from the EDX results, samples from Ag/Pt molar ratios of 1/2, 2/2, and 3/2 show a complete reduction of Pt. This can be seen by the linear relationship between the volume of silver nitrate and the Ag/Pt molar ratio for all the samples with a Ag/Pt molar ratio above 1/2. Thus, AA is not only reducing Ag^+ but is also reducing $PtCl_4^{2-}$.

When HQ is used as the reducing agent, using Ag/Pt = 1/2 and the associated thin Ag shell, the HQ shows some reduction capability to form some fuzzy spikes (Figure 3a). However, in all the samples using HQ, the GRRs dominate and hence all the samples have a hollow shell structure. In addition, because the HQ has weak or no reducing capability in this context, the Ag^+ generated via the galvanic reaction will form AgCl with Cl^+ [reaction (4)] when the concentrations of ions are high enough. The representative SEM image of the sample with highest molar ratio (Ag/Pt = 20/2) fabricated with HQ (Figure 8c), shows very clear AgCl crystals (one example is indicated by the yellow box) and this yellow box area was also investigated via EDX which further confirms that the observed crystal is formed from the elements Ag and Cl (Figure 8d and Figure S9b).

Catalytic Reduction of 4-NP Using Fabricated Catalysts. *Catalytic Reduction of 4-NP.* Nitrophenols (NPs), including para-, meta-, and *ortho*-nitrophenol, are one kind of hazardous and toxic pollutant derived from the manufacture of pesticides, pharmaceutical, and synthetic dyes.[64,65] It is critical to remove the soluble and stable nitrophenols efficiently and completely from wastewater. In addition, the reduction of 4-NP by $NaBH_4$ in an aqueous solution is a well-known and easily monitored reaction. Thus, it was chosen as a model reaction to test the catalytic activity of the fabricated nanomaterials.[66,67] The reaction, as the insert in Figure 9, monitored by collecting the UV−vis absorption

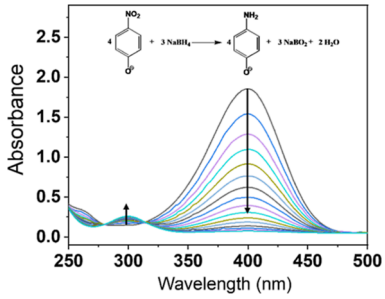

Figure 9. Time-dependent UV−vis absorption spectra of 4-NP reduced by $NaBH_4$ and catalyzed by the Pt-based metallic catalysis.

spectrum of the mixture of 4-NP and $NaBH_4$ at different times. As an example, Figure 9 shows time-dependent UV−vis absorption spectra of the 4-NP solution (3 mM, 100 μL) mixed with 100 μL of as-purified nanocatalysts in 2.8 mL of nanopure water. Each spectrum was recorded 2 min after the prior spectrum. Initially, the solution showed an absorption peak at ∼400 nm due to the formation of 4-nitrophenolate ions which is caused by the addition of $NaBH_4$ solutions. With the addition of a catalyst, the absorption peak at ∼400 nm decreases and a new peak at 315 nm associated with $-NH_2$ of 4-aminophenol (4-AP), appeared and increased with the reaction time, which demonstrates that the 4-NP has been rapidly and effectively reduced to 4-AP under the acceleration of catalysts.

During the reaction, the presence of $NaBH_4$ in the nitrophenol solution resulted in the deprotonation of nitrophenol to nitrophenolate ions which were adsorbed on the surface of the catalyst via nitro groups. The electrons generated from the reaction of BH^{4-} and H^+ transferred to nitrophenolate ions through the unique electronic structure of the nanostructure, and the nitrophenolate ions received electrons to form aminophenol. The kinetic reaction rate (k) could be evaluated by a pseudo-first-order kinetics which could be estimated from the plot of $\ln(A_0/A_t)$ versus the reaction time, in which A is the absorption at 400 nm, while A_0 and A_t are the absorbance at the initial stage and successive intervals, respectively.

Catalytical Performance of Fabricated Nanocatalysts. Figures S11 and S12 show the representative time-dependent UV−vis absorption spectra of the 4-NP solution mixed with all the nanocatalysts obtained with each of HQ and AA. $Ln(A_0/A_t)$ as a function of reaction time for all the structures are depicted to facilitate direct comparison of catalytic activity between those nanostructures. The same catalytic reactions

https://doi.org/10.1021/acs.chemmater.2c02659
Chem. Mater. 2022, 34, 9282−9293

were repeated more than 5 times to get more reliable data. The average rate of each reaction can be plotted using the linear fit equation $\ln(A_0/A_t) = kt$.

Figure 10a shows a representative plot of $\ln(A_0/A_t)$ as a function of reaction time for all the structures fabricated with

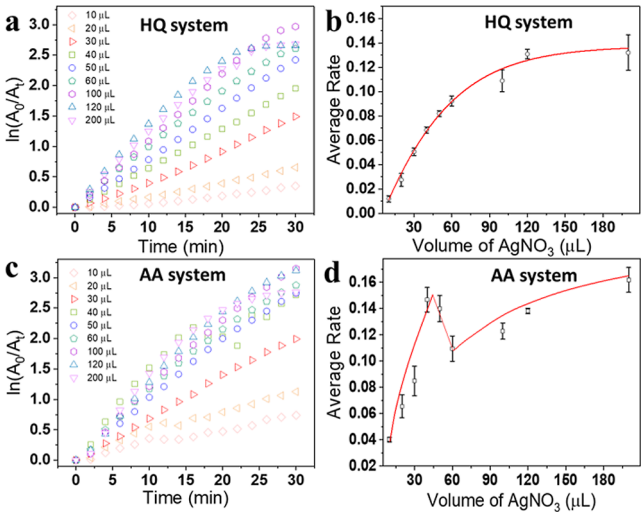

Figure 10. (a) Graph of $\ln(A_0/A_t)$ as a function of reaction time giving the comparative rate constants of all the structures fabricated with HQ. (b) Plot of the average reaction rate as a function of the amount of $AgNO_3$ that was used for the nanocatalysts fabricated with HQ. (c) Graph of $\ln(A_0/A_t)$ as a function of reaction time giving the comparative rate constants of all the structures fabricated with AA. (d) Plot of the average reaction rate as a function of the amount of $AgNO_3$ that was used for the nanocatalysts fabricated with AA.

HQ. With increased volume of $AgNO_3$, the reaction rate is gradually increased. The samples made with the largest amount of $AgNO_3$, 120 and 200 μL, have very similar reaction rates, as shown by the blue and pink triangles in Figure 10a, indicating that it has reached the catalytic activity plateau. Figure 10b plots the average reaction rate as a function of $AgNO_3$ volume. Consistent with Figure 10a, the average rate increases gradually with the increase in $AgNO_3$ volume until the volume of $AgNO_3$ is up to approximately 100 μL and such a trend can be nicely fit with an exponential growth curve. This indicates that the catalysis performance increases as the shell volume increases and eventually reaches a plateau. This is not surprising because the hollow shell structure is gradually enlarged, which increases the total surface area along with the number of potential reaction sites, which will enhance the catalytic activity.[68,69]

For the nanocatalysts synthesized with AA, $\ln(A_0/A_t)$ as a function of reaction time is depicted in Figure 10c. The average reaction rate value as a function of $AgNO_3$ volume is plotted in Figure 10d. It provides a clear trend on how the reaction rate changes over the $AgNO_3$ volume range. At the beginning, the reaction rate has dramatically increased up to samples made in 40 μL of $AgNO_3$ volume. Such increased catalytic activity is possible as a result of the increased surface area, chemical composition, and the morphology from formed spiky branches for those samples.[70−75] However, such spiky branches start to decrease around the nanocatalysts made with 50 μL $AgNO_3$ which results in the decreased catalytic activity. With the further increased $AgNO_3$ volume, the hollow shell structure is gradually enlarged, while the overall surface area continues to increase, resulting in increased catalytic activity. In addition, the catalytic activity could also be impacted by the absorbed ligands on the surface of catalysis material. It has been reported that citric acid can significantly improve the Pt monolayer shell as the absorbing surfactant during the reaction by the Shao group.[76] Thus, in the future, it would be desirable to investigate whether AA as a surfactant plays a significant role in catalytic activity.

■ CONCLUSIONS

In summary, a mesoporous silica ($mSiO_2$) shell-supported AuNDB nanostructure was first synthesized using seeds for silver shell deposition. Due to the porous structure of $mSiO_2$, silver ions were able to penetrate through the shell of silica and deposit on the Au surface, forming AuNDB@Ag@$mSiO_2$. The Ag deposition behavior and impacts on nanostructure properties when using various amounts of Ag^+ were discussed. With the fabricated AuNDB@Ag@$mSiO_2$ nanostructures, HQ and AA were used separately to assist the GRR between the Pt precursor and the Ag sacrificial template. With various thicknesses of silver shells and the varying strength of the reducing agent, the rates of co-reduction and GRRs in each system could be manipulated, impacting the final morphology and composition of the Pt-based catalysts. This catalysis study suggests that the total surface area and the composition of the Ag/Pt alloy can influence the reactivity significantly. Our work advances the rational design of efficient, low-cost catalysts for redox processes.

■ EXPERIMENTAL SECTION

Materials. Hexadecyltrimethylammonium bromide (CTAB), gold (III) chloride trihydrate ($HAuCl_4{\cdot}3H_2O$), potassium tetrachloroplatinate(II) (K_2PtCl_4), potassium iodide (KI), L-ascorbic acid (L-AA), HQ, sodium borohydride ($NaBH_4$), polyvinylpyrrolidone (PVP, MW: 55,000), sodium citrate, tetraethyl orthosilicate (TEOS), ammonium hydroxide (NH_4OH), 4-NP, and ethanol (EtOH) were all purchased from Sigma-Aldrich. Silver nitrate ($AgNO_3$) was purchased from Fisher Scientific. All chemicals were used as received without further purification.

Synthesis of AuNDBs. The synthesis method via the iodide-mediated growth of AuNDBs is obtained following the protocol with slight modification from the Liz-Marzán group.[49] The starting GNRs were synthesized via a slight modification to the seed-mediated growth method.

To prepare the seeds, 0.250 mL of 0.01 M $HAuCl_4$ was added to 10.0 mL of 0.1 M CTAB. 0.600 mL of 0.01 M $NaBH_4$ was then added. The solution color changed from orange to light brown, indicating the formation of gold seeds. The solution was stirred for 2 min and left to stand for 2 h. For the growth solution, a solution of surfactants was first prepared by dissolving 1.445 g of CTAB into 40 mL nanopure water at 45 °C and cooled down to room temperature before use. Then, 2.0 mL of 0.01 M $HAuCl_4$ and 0.800 mL of 1 M HCl were added to the surfactant solution and shaken for 30 s. This was followed by the addition of 0.400 mL of 0.01 M $AgNO_3$ and 0.320 mL of 0.1 M L-AA and shaken for another 30 s. Finally, 0.096 mL of Au seed solution was added and the solution was shaken for 30 s and then left in a 35 °C water bath for at least 16 h for the completion of AuNR growth.

In order to synthesize AuNDBs, the 10 mL as-synthesized AuNRs were centrifuged and washed twice in nanopure water at 11,000 rpm for 8 min. Then, the purified AuNRs were redispersed in a 2 mL, 10 mM aqueous CTAB solution for further use.

A solution was prepared by mixing 10.0 mL, 10 mM CTAB aqueous CTAB and 50 μL, 0.05 M $HAuCl_4{\cdot}3H_2O$. The solution was kept at room temperature for 5 min before adding 5.7 μL of 0.01 M KI and 40 μL of 0.1 M L-AA. Finally, 600 μL of AuNRs that prepared

https://doi.org/10.1021/acs.chemmater.2c02659
Chem. Mater. 2022, 34, 9282−9293

earlier was then added into the mixture solution under stirring. The whole solution was stirred for 1 h. The resultant AuNDBs were centrifuged and redispersed in nanopure water at 8,000 rpm for 8 min before silica shell coating or further characterization.

Synthesis of AuNDBs@SiO_2. The as-synthesized AuNDBs were centrifuged at 8,000 rpm for 8 min, and the precipitates were redispersed in an aqueous CTAB solution (10 mL, 9 mM). Under gentle stirring, aqueous NH_4OH (150 μL, 0.01 M) was added to adjust pH to 10.4, followed by three sequential additions of TEOS in EtOH [10 μL, 20% (v/v)] with 30 min intervals in between additions. The solution was then left under stirring conditions for 24 h at room temperature. The as-prepared AuNDBs@SiO_2 were centrifuged and washed twice in EtOH at 8,000 rpm for 8 min. After that, the sample was ready for the deposition of the Ag shell and further characterization. With the presented amount of TEOS, the formed $mSiO_2$ shell thickness is approximately 19 nm, which was measured on either side of AuNDBs.

Preparation of AuNDBs@Ag@SiO_2. The as-purified AuNDBs@SiO_2 (1 mL) was dispersed in an aqueous PVP solution (1 mL, 70.4 mg). Under stirring, various volumes of 0.01 M $AgNO_3$ (10, 20, 30, 40, 50, 60, 100, 120, and 200 μL) were added, followed by the addition of HQ (140 μL, 0.01 M) and allowed to stir for 1 h and sat undisturbed for 12 h. The solution was then centrifuged and washed twice in EtOH at 8000 rpm for 8 min before the deposition of Pt shell and characterization. The calculated Au/Ag molar ratio is $15/x$, (x = 1, 2, 3, 4, 5, 6, 10, 12, and 20).

Preparation of Silica-Coated AuNDBs@Pt@SiO_2 Nanocatalysts. After the initial purification of AuNDBs@Ag@SiO_2 at various volumes of $AgNO_3$, the precipitate was dispersed in an aqueous PVP solution (1 mL, 70.4 mg). Under stirring, K_2PtCl_4 (20 μL, 0.01 M) and two different reducing agents, L-AA (40 μL, 0.1 M) and HQ (40 μL, 0.01 M), were added to yield different morphological nanocatalysts. The solution was stirred for 5 min and sat undisturbed for 12 h. The solution was then centrifuged and washed twice in nanopure water at 8000 rpm for 8 min before the catalytic reduction of 4-NP and any characterization. The calculated Ag/Pt molar ratio is $x/2$, (x = 1, 2, 3, 4, 5, 6, 10, 12, and 20).

Catalytic Reduction of 4-Nitrophenol. The catalytic properties of silica-coated hollow AuNDBs@Pt nanocatalysts were studied by in situ UV−vis monitoring the change in absorption of 4-NP in the presence of $NaBH_4$ at 400 nm. In a typical catalysis experiment, nanopure water (2.8 mL) was added into a quartz cuvette, followed by the addition of an aqueous solution of 4-NP (100 μL, 0.003 M) and the as-purified AuNDBs@Pt@SiO_2 nanocatalysts (100 μL). Upon beginning in situ monitoring, freshly prepared ice cold $NaBH_4$ (100 μL, 0.3 M) was added. The catalytic reduction was monitored by observing the change in absorption at a wavelength peak of 400 nm with a 1 min interval over a span of 30 min with the use of the UV−vis spectrophotometer.

Instruments and Measurement. STEM imaging, EDX spectroscopy, and elemental mapping were conducted using a JOEL-7200F field emission scanning electron microscope operated at 30 kV. HRTEM images and high-resolution EDX mapping of the individual nanostructure were obtained using a FEI Tecnai F20 instrument (Thermo Fisher Scientific) operated at 200 kV. The XPS measurements were performed on a Surface Science Instruments M Probe ESCA spectrometer with a 200 watt monochromatic Al Kα X-ray source, hemispherical analyzer, and a take-off angle of 55° with respect to vertical. All the material sizes were measured via STEM images by ImageJ software. The STEM samples were prepared by drop-casting samples onto copper grids. UV−vis absorption spectra were recorded using a Jasco V 670 UV−Vis−NIR spectrophotometer.

■ ASSOCIATED CONTENT

Supporting Information

The Supporting Information is available free of charge at https://pubs.acs.org/doi/10.1021/acs.chemmater.2c02659.

Detailed discussion on the possible mechanism of fabricating AuNDBs by using AuNRs; UV−vis absorption spectra of AuNRs, AuNDB, AuNDB@$mSiO_2$, and AuNDB@Ag@$mSiO_2$ and their spectra change discussion; UV−vis spectra of the nanostructure before and after the galvanic reaction using HQ-coupled GRR between the Pt precursor and silver shell which is from the AuNDB@Ag@$mSiO_2$ made with 20 μL of $AgNO_3$; representative STEM images of HQ-assisted Pt-based nanocatalysis using AuNDB@Ag@$mSiO_2$ made with various amounts of $AgNO_3$; the UV−Vis spectra of the nanostructure before and after the galvanic reaction using AA-coupled GRR between the Pt precursor and silver shell which is from the AuNDB@Ag@$mSiO_2$ made with 20 μL of $AgNO_3$; HRTEM image and lattice fringe of AA-assisted Pt-based nanocatalysis using AuNDB@Ag@$mSiO_2$ under GRR; XPS spectrum of Ag 3d and Pt 4d of AA-assisted Pt-based nanocatalysis using AuNDB@Ag@$mSiO_2$ made with 30 μL of $AgNO_3$ (Ag/Pt = 3/2); representative STEM images of AA-assisted Pt-based nanocatalysis using AuNDB@Ag@mSiO2 made with various amounts of $AgNO_3$; reaction kinetic UV−vis spectra of forming samples with molar ratio of Ag/Pt = 3/2, 5/2 and the summarized peak intensity value change plots as the function of reaction time; EDX spectra of samples with highest molar ratio (Ag/Pt = 20/2) prepared under AA- or HQ-assisted GRR; plot of Ag/Pt atomic ratio as the function of the silver nitrate volume with AA as reducing agent; and representative time-dependent UV−vis absorption spectra of the 4-NP solution mixed with all the nanocatalysts obtained with HQ and AA (PDF)

■ AUTHOR INFORMATION

Corresponding Author

Ying Bao − *Department of Chemistry, Western Washington University, Bellingham, Washington 98225, United States;* orcid.org/0000-0001-9780-642X; Email: ying.bao@wwu.edu

Authors

John R. Crockett − *Department of Chemistry, Western Washington University, Bellingham, Washington 98225, United States*

Maggie Wang − *Department of Chemistry, Western Washington University, Bellingham, Washington 98225, United States*

Joseph E. Doebler − *Department of Chemistry, Western Washington University, Bellingham, Washington 98225, United States*

Tejal Pawale − *Materials Science and Engineering Department, University of North Texas, Denton, Texas 76207, United States*

Xiao Li − *Materials Science and Engineering Department, University of North Texas, Denton, Texas 76207, United States;* orcid.org/0000-0003-3456-1933

Complete contact information is available at: https://pubs.acs.org/10.1021/acs.chemmater.2c02659

Notes

The authors declare no competing financial interest.

■ ACKNOWLEDGMENTS

This research was supported by Western Washington University, Department of Chemistry. STEM studies were conducted on an instrument funded by the Joint Center for Deployment and Research in Earth Abundant Materials (JCDREAM). J.R.C.'s contributions were partially supported by the National Science Foundation (grant no. 2108842). J.E.D. thanks the partial support from the RSP graduate award from Western Washington University. The authors are grateful to Alexandra Hoff and Bryce Pettit Estell for their help on data analysis, as well as all members in Bao group for valuable discussions.

■ REFERENCES

(1) Moiseev, I. Catalysis: 2000 AD1. *Kinet. Catal.* **2001**, *42*, 1−22.

(2) Voltz, S. E.; Morgan, C. R.; Liederman, D.; Jacob, S. M. Kinetic Study of Carbon Monoxide and Propylene Oxidation on Platinum Catalysts. *Ind. Eng. Chem. Prod. Res. Dev.* **1973**, *12*, 294−301.

(3) Gasteiger, H. A.; Kocha, S. S.; Sompalli, B.; Wagner, F. T. Activity benchmarks and requirements for Pt, Pt-alloy, and non-Pt oxygen reduction catalysts for PEMFCs. *Appl. Catal., B* **2005**, *56*, 9−35.

(4) Burch, R.; Breen, J. P.; Meunier, F. C. A review of the selective reduction of NOx with hydrocarbons under lean-burn conditions with non-zeolitic oxide and platinum group metal catalysts. *Appl. Catal., B* **2002**, *39*, 283−303.

(5) Li, L.; Larsen, A. H.; Romero, N. A.; Morozov, V. A.; Glinsvad, C.; Abild-Pedersen, F.; Greeley, J.; Jacobsen, K. W.; Nørskov, J. K. Investigation of Catalytic Finite-Size-Effects of Platinum Metal Clusters. *J. Phys. Chem. Lett.* **2013**, *4*, 222−226.

(6) Lopes, P. P.; Li, D.; Lv, H.; Wang, C.; Tripkovic, D.; Zhu, Y.; Schimmenti, R.; Daimon, H.; Kang, Y.; Snyder, J.; Becknell, N.; More, K. L.; Strmcnik, D.; Markovic, N. M.; Mavrikakis, M.; Stamenkovic, V. R. Eliminating dissolution of platinum-based electrocatalysts at the atomic scale. *Nat. Mater.* **2020**, *19*, 1207−1214.

(7) Liang, Z.; Song, L.; Elnabawy, A. O.; Marinkovic, N.; Mavrikakis, M.; Adzic, R. R. Platinum and Palladium Monolayer Electrocatalysts for Formic Acid Oxidation. *Top. Catal.* **2020**, *63*, 742−749.

(8) Yang, L.; Vukmirovic, M. B.; Su, D.; Sasaki, K.; Herron, J. A.; Mavrikakis, M.; Liao, S.; Adzic, R. R. Tuning the Catalytic Activity of Ru@Pt Core-Shell Nanoparticles for the Oxygen Reduction Reaction by Varying the Shell Thickness. *J. Phys. Chem. C* **2013**, *117*, 1748−1753.

(9) Yuan, Q.; Wakisaka, Y.; Uemura, Y.; Wada, T.; Ariga-Miwa, H.; Takakusagi, S.; Asakura, K.; Brankovic, S. R. Reaction Stoichiometry and Mechanism of Pt Deposition via Surface Limited Redox Replacement of Copper UPD Layer on Au(111). *J. Phys. Chem. C* **2018**, *122*, 16664−16673.

(10) Xie, Y.; Yang, Y.; Muller, D. A.; Abruña, H. D.; Dimitrov, N.; Fang, J. Enhanced ORR Kinetics on Au-Doped Pt-Cu Porous Films in Alkaline Media. *ACS Catal.* **2020**, *10*, 9967−9976.

(11) Xie, Y.; Li, C.; Razek, S. A.; Fang, J.; Dimitrov, N. Synthesis of Nanoporous Au−Cu−Pt Alloy as a Superior Catalyst for the Methanol Oxidation Reaction. *ChemElectroChem* **2020**, *7*, 569−580.

(12) Xie, Y.; Dimitrov, N. Ultralow Pt loading nanoporous Au-Cu-Pt thin film as highly active and durable catalyst for formic acid oxidation. *Appl. Catal., B* **2020**, *263*, 118366.

(13) Yuan, Q.; Doan, H. A.; Grabow, L. C.; Brankovic, S. R. Finite Size Effects in Submonolayer Catalysts Investigated by CO Electrosorption on PtsML/Pd(100). *J. Am. Chem. Soc.* **2017**, *139*, 13676−13679.

(14) Pizzutilo, E.; Geiger, S.; Grote, J. P.; Mingers, A.; Mayrhofer, K. J. J.; Arenz, M.; Cherevko, S. On the Need of Improved Accelerated Degradation Protocols (ADPs): Examination of Platinum Dissolution and Carbon Corrosion in Half-Cell Tests. *J. Electrochem. Soc.* **2016**, *163*, F1510−F1514.

(15) Shao-Horn, Y.; Sheng, W. C.; Chen, S.; Ferreira, P. J.; Holby, E. F.; Morgan, D. Instability of Supported Platinum Nanoparticles in Low-Temperature Fuel Cells. *Top. Catal.* **2007**, *46*, 285−305.

(16) Ferreira, P. J.; la O', G. J.; Morgan, Y.; Makharia, D.; Kocha, R.; Gasteiger, S.; Gasteiger, H. A. Instability of Pt/C Electrocatalysts in Proton Exchange Membrane Fuel Cells. *J. Electrochem. Soc.* **2005**, *152*, A2256.

(17) de Bruijn, F. A.; Dam, V. A. T.; Janssen, G. J. M. Review: Durability and Degradation Issues of PEM Fuel Cell Components. *Fuel Cells* **2008**, *8*, 3−22.

(18) Bai, L.; Wang, X.; Chen, Q.; Ye, Y.; Zheng, H.; Guo, J.; Yin, Y.; Gao, C. Explaining the Size Dependence in Platinum-Nanoparticle-Catalyzed Hydrogenation Reactions. *Angew. Chem., Int. Ed.* **2016**, *55*, 15656−15661.

(19) Lee, H.; Habas, S. E.; Kweskin, S.; Butcher, D.; Somorjai, G. A.; Yang, P. Morphological Control of Catalytically Active Platinum Nanocrystals. *Angew. Chem., Int. Ed.* **2006**, *45*, 7824−7828.

(20) Narayanan, R.; El-Sayed, M. A. Shape-Dependent Catalytic Activity of Platinum Nanoparticles in Colloidal Solution. *Nano Lett.* **2004**, *4*, 1343−1348.

(21) Tominaka, S.; Nakamura, Y.; Osaka, T. Nanostructured catalyst with hierarchical porosity and large surface area for on-chip fuel cells. *J. Power Sources* **2010**, *195*, 1054−1058.

(22) Xiao, M.; Wang, Z.; Lyu, M.; Luo, B.; Wang, S.; Liu, G.; Cheng, H.-M.; Wang, L. Hollow Nanostructures for Photocatalysis: Advantages and Challenges. *Adv. Mater.* **2019**, *31*, 1801369.

(23) Cohen-Pope, S.; Crockett, J. R.; Wang, M.; Flynn, K.; Hoff, A.; Bao, Y. Morphology control of SERS-active 2D gold nanosnowflakes. *J. Mater. Chem. C* **2020**, *8*, 12427−12436.

(24) Alayoglu, S.; Nilekar, A. U.; Mavrikakis, M.; Eichhorn, B. Ru-Pt core-shell nanoparticles for preferential oxidation of carbon monoxide in hydrogen. *Nat. Mater.* **2008**, *7*, 333−338.

(25) Wang, J.; Loh, K. P.; Zhong, Y. L.; Lin, M.; Ding, J.; Foo, Y. L. Bifunctional FePt Core−Shell and Hollow Spheres: Sonochemical Preparation and Self-Assembly. *Chem. Mater.* **2007**, *19*, 2566−2572.

(26) Zeng, J.; Yang, J.; Lee, J. Y.; Zhou, W. Preparation of Carbon-Supported Core−Shell Au−Pt Nanoparticles for Methanol Oxidation Reaction: The Promotional Effect of the Au Core. *J. Phys. Chem. B* **2006**, *110*, 24606−24611.

(27) Ruditskiy, A.; Choi, S.-I.; Peng, H.-C.; Xia, Y. Shape-controlled metal nanocrystals for catalytic applications. *MRS Bull.* **2014**, *39*, 727−737.

(28) Chen, S.; Thota, S.; Singh, G.; Aímola, T. J.; Koenigsmann, C.; Zhao, J. Synthesis of hollow Pt-Ag nanoparticles by oxygen-assisted acid etching as electrocatalysts for the oxygen reduction reaction. *RSC Adv.* **2017**, *7*, 46916−46924.

(29) Chen, S.; Thota, S.; Wang, X.; Zhao, J. From solid to core@shell to hollow Pt-Ag nanocrystals: thermally controlled surface segregation to enhance catalytic activity and durability. *J. Mater. Chem. A* **2016**, *4*, 9038−9043.

(30) Tan, C.; Sun, Y.; Zheng, J.; Wang, D.; Li, Z.; Zeng, H.; Guo, J.; Jing, L.; Jiang, L. A self-supporting bimetallic Au@Pt core-shell nanoparticle electrocatalyst for the synergistic enhancement of methanol oxidation. *Sci. Rep.* **2017**, *7*, 6347.

(31) Singh, B.; Seddon, B.; Dempsey, E.; Redington, W.; Dickinson, C. Porous Core-Shell Platinum-Silver Nanocatalyst for the Electro-oxidation of Methanol. *Electroanalysis* **2015**, *27*, 135−143.

(32) Daniel, J. R.; McCarthy, L. A.; Ringe, E.; Boudreau, D. Enhanced control of plasmonic properties of silver−gold hollow nanoparticles via a reduction-assisted galvanic replacement approach. *RSC Adv.* **2019**, *9*, 389−396.

(33) Xia, X.; Wang, Y.; Ruditskiy, A.; Xia, Y. 25th Anniversary Article: Galvanic Replacement: A Simple and Versatile Route to Hollow Nanostructures with Tunable and Well-Controlled Properties. *Adv. Mater.* **2013**, *25*, 6313−6333.

(34) Sun, Y.; Xia, Y. Shape-Controlled Synthesis of Gold and Silver Nanoparticles. *Science* **2002**, *298*, 2176−2179.

(35) Wiley, B.; Sun, Y.; Chen, J.; Cang, H.; Li, Z.-Y.; Li, X.; Xia, Y. Shape-Controlled Synthesis of Silver and Gold Nanostructures. *MRS Bull.* **2005**, *30*, 356−361.
(36) Bansal, V.; O'Mullane, A.; Bhargava, S. Galvanic replacement mediated synthesis of hollow Pt nanocatalysts: Significance of residual Ag for the H2 evolution reaction. *Electrochem. Commun.* **2009**, *11*, 1639−1642.
(37) Yang, X.; Roling, L. T.; Vara, M.; Elnabawy, A. O.; Zhao, M.; Hood, Z. D.; Bao, S.; Mavrikakis, M.; Xia, Y. Synthesis and Characterization of Pt-Ag Alloy Nanocages with Enhanced Activity and Durability toward Oxygen Reduction. *Nano Lett.* **2016**, *16*, 6644−6649.
(38) Chen, J.; Wiley, B.; McLellan, J.; Xiong, Y.; Li, Z.-Y.; Xia, Y. Optical Properties of Pd−Ag and Pt−Ag Nanoboxes Synthesized via Galvanic Replacement Reactions. *Nano Lett.* **2005**, *5*, 2058−2062.
(39) Lee, C.-L.; Tseng, C.-M. Ag−Pt Nanoplates: Galvanic Displacement Preparation and Their Applications As Electrocatalysts. *J. Phys. Chem. C* **2008**, *112*, 13342−13345.
(40) Zhang, W.; Yang, J.; Lu, X. Tailoring Galvanic Replacement Reaction for the Preparation of Pt/Ag Bimetallic Hollow Nanostructures with Controlled Number of Voids. *ACS Nano* **2012**, *6*, 7397−7405.
(41) Zhang, H.; Jin, M.; Wang, J.; Li, W.; Camargo, P. H. C.; Kim, M. J.; Yang, D.; Xie, Z.; Xia, Y. Synthesis of Pd−Pt Bimetallic Nanocrystals with a Concave Structure through a Bromide-Induced Galvanic Replacement Reaction. *J. Am. Chem. Soc.* **2011**, *133*, 6078−6089.
(42) Ye, F.; Liu, H.; Hu, W.; Zhong, J.; Chen, Y.; Cao, H.; Yang, J. Heterogeneous Au-Pt nanostructures with enhanced catalytic activity toward oxygen reduction. *Dalton Trans.* **2012**, *41*, 2898−2903.
(43) Merkoçi, F.; Patarroyo, J.; Russo, L.; Piella, J.; Genç, A.; Arbiol, J.; Bastús, N. G.; Puntes, V. Understanding galvanic replacement reactions: the case of Pt and Ag. *Mater. Today Adv.* **2020**, *5*, 100037.
(44) Bordley, J. A.; El-Sayed, M. A. Enhanced Electrocatalytic Activity toward the Oxygen Reduction Reaction through Alloy Formation: Platinum-Silver Alloy Nanocages. *J. Phys. Chem. C* **2016**, *120*, 14643−14651.
(45) Rodrigues, T. S.; da Silva, A. G. M.; Gonçalves, M. C.; Fajardo, H. V.; Balzer, R.; Probst, L. F. D.; Camargo, P. H. C. AgPt Hollow Nanodendrites: Synthesis and Uniform Dispersion over SiO2Support for Catalytic Applications. *ChemNanoMat* **2015**, *1*, 46−51.
(46) Rodrigues, T. S.; da Silva, A. H. M.; da Silva, A. G. M.; Ceara, D. G.; Gomes, J. F.; Assaf, J. M.; Camargo, P. H. C. Hollow AgPt/SiO2 nanomaterials with controlled surface morphologies: is the number of Pt surface atoms imperative to optimize catalytic performances? *Catal. Sci. Technol.* **2016**, *6*, 2162−2170.
(47) Crockett, J. R.; Win-Piazza, H.; Doebler, J. E.; Luan, T.; Bao, Y. Plasmonic Detection of Mercury via Amalgamation on Gold Nanorods Coated with PEG-Thiol. *ACS Appl. Nano Mater.* **2021**, *4*, 1654−1663.
(48) Wang, M.; Hoff, A.; Doebler, J. E.; Emory, S. R.; Bao, Y. Dumbbell-Like Silica Coated Gold Nanorods and Their Plasmonic Properties. *Langmuir* **2019**, *35*, 16886−16892.
(49) Grzelczak, M.; Sánchez-Iglesias, A.; Rodríguez-González, B.; Alvarez-Puebla, R.; Pérez-Juste, J.; Liz-Marzán, L. M. Influence of Iodide Ions on the Growth of Gold Nanorods: Tuning Tip Curvature and Surface Plasmon Resonance. *Adv. Funct. Mater.* **2008**, *18*, 3780−3786.
(50) Fernanda Cardinal, M.; Rodríguez-González, B.; Alvarez-Puebla, R. A.; Pérez-Juste, J.; Liz-Marzán, L. M. Modulation of Localized Surface Plasmons and SERS Response in Gold Dumbbells through Silver Coating. *J. Phys. Chem. C* **2010**, *114*, 10417−10423.
(51) Tebbe, M.; Kuttner, C.; Mayer, M.; Maennel, M.; Pazos-Perez, N.; König, T. A. F.; Fery, A. Silver-Overgrowth-Induced Changes in Intrinsic Optical Properties of Gold Nanorods: From Noninvasive Monitoring of Growth Kinetics to Tailoring Internal Mirror Charges. *J Phys Chem C Nanomater Interfaces* **2015**, *119*, 9513−9523.
(52) Gómez-Graña, S.; Goris, B.; Altantzis, T.; Fernández-López, C.; Carbó-Argibay, E.; Guerrero-Martínez, A.; Almora-Barrios, N.; López, N.; Pastoriza-Santos, I.; Pérez-Juste, J.; Bals, S.; Van Tendeloo, G.; Liz-Marzán, L. M. Au@Ag Nanoparticles: Halides Stabilize {100} Facets. *J. Phys. Chem. Lett.* **2013**, *4*, 2209−2216.
(53) Sánchez-Iglesias, A.; Carbó-Argibay, E.; Glaria, A.; Rodríguez-González, B.; Pérez-Juste, J.; Pastoriza-Santos, I.; Liz-Marzán, L. M. Rapid Epitaxial Growth of Ag on Au Nanoparticles: From Au Nanorods to Core−Shell Au@Ag Octahedrons. *Chem.—Eur. J.* **2010**, *16*, 5558−5563.
(54) Becker, J.; Zins, I.; Jakab, A.; Khalavka, Y.; Schubert, O.; Sönnichsen, C. Plasmonic Focusing Reduces Ensemble Linewidth of Silver-Coated Gold Nanorods. *Nano Lett.* **2008**, *8*, 1719−1723.
(55) Viswanath, B.; Kundu, P.; Halder, A.; Ravishankar, N. Mechanistic Aspects of Shape Selection and Symmetry Breaking during Nanostructure Growth by Wet Chemical Methods. *J. Phys. Chem. C* **2009**, *113*, 16866−16883.
(56) Lai, Y.; Du, G.; Zheng, Z.; Dong, Y.; Li, H.; Kuang, Q.; Xie, Z. Facile synthesis of clean PtAg dendritic nanostructures with enhanced electrochemical properties. *Inorg. Chem. Front.* **2020**, *7*, 1250−1256.
(57) Huang, M.; Zhang, H.; Yin, S.; Zhang, X.; Wang, J. PtAg Alloy Nanoparticles Embedded in Polyaniline as Electrocatalysts for Formate Oxidation and Hydrogen Evolution. *ACS Appl. Nano Mater.* **2020**, *3*, 3760−3766.
(58) Sui, N.; Wang, K.; Shan, X.; Bai, Q.; Wang, L.; Xiao, H.; Liu, M.; Colvin, V. L.; Yu, W. W. Facile synthesis of hollow dendritic Ag/Pt alloy nanoparticles for enhanced methanol oxidation efficiency. *Dalton Trans.* **2017**, *46*, 15541−15548.
(59) Fu, T.; Fang, J.; Wang, C.; Zhao, J. Hollow porous nanoparticles with Pt skin on a Ag-Pt alloy structure as a highly active electrocatalyst for the oxygen reduction reaction. *J. Mater. Chem. A* **2016**, *4*, 8803−8811.
(60) Kalyan, I.; Pal, T.; Pal, A. Time and temperature dependent formation of hollow gold nanoparticles via galvanic replacement reaction of As(0) and its catalytic application. *MRS Commun.* **2019**, *9*, 270−279.
(61) Xia, X.; Wang, Y.; Ruditskiy, A.; Xia, Y. 25th anniversary article: galvanic replacement: a simple and versatile route to hollow nanostructures with tunable and well-controlled properties. *Adv. Mater.* **2013**, *25*, 6313−6333.
(62) Matsui, T.; Kitagawa, Y.; Okumura, M.; Shigeta, Y. Accurate Standard Hydrogen Electrode Potential and Applications to the Redox Potentials of Vitamin C and NAD/NADH. *J. Phys. Chem. A* **2015**, *119*, 369−376.
(63) Yadav, A. P.; Sugawara, Y.; Nishikata, A.; Tsuru, T. Electrochemical Stability and Oxidation Mechanism of Carbon Support for PEM Fuel Cell. *ECS Trans.* **2008**, *16*, 2093−2099.
(64) Ismail, M.; Khan, M. I.; Khan, S. B.; Akhtar, K.; Khan, M. A.; Asiri, A. M. Catalytic reduction of picric acid, nitrophenols and organic azo dyes via green synthesized plant supported Ag nanoparticles. *J. Mol. Liq.* **2018**, *268*, 87−101.
(65) Albukhari, S. M.; Ismail, M.; Akhtar, K.; Danish, E. Y. Catalytic reduction of nitrophenols and dyes using silver nanoparticles @ cellulose polymer paper for the resolution of waste water treatment challenges. *Colloids Surf. A Phyusicochem. Eng.* **2019**, *577*, 548−561.
(66) Iben Ayad, A.; Luart, D.; Ould Dris, A.; Guénin, E. Kinetic Analysis of 4-Nitrophenol Reduction by "Water-Soluble" Palladium Nanoparticles. *Nanomaterials* **2020**, *10*, 1169.
(67) Gu, S.; Lu, Y.; Kaiser, J.; Albrecht, M.; Ballauff, M. Kinetic analysis of the reduction of 4-nitrophenol catalyzed by Au/Pd nanoalloys immobilized in spherical polyelectrolyte brushes. *Phys. Chem. Chem. Phys.* **2015**, *17*, 28137−28143.
(68) Sun, S.; Li, H.; Xu, Z. J. Impact of Surface Area in Evaluation of Catalyst Activity. *Joule* **2018**, *2*, 1024−1027.
(69) Dignon, G. L.; Zheng, W.; Kim, Y. C.; Mittal, J. Temperature-Controlled Liquid-Liquid Phase Separation of Disordered Proteins. *ACS Cent. Sci.* **2019**, *5*, 821−830.
(70) Peng, Z.; You, H.; Yang, H. An Electrochemical Approach to PtAg Alloy Nanostructures Rich in Pt at the Surface. *Adv. Funct. Mater.* **2010**, *20*, 3734−3741.

(71) Jiang, X.; Fu, G.; Wu, X.; Liu, Y.; Zhang, M.; Sun, D.; Xu, L.; Tang, Y. Ultrathin AgPt alloy nanowires as a high-performance electrocatalyst for formic acid oxidation. *Nano Res.* **2018**, *11*, 499−510.

(72) Zhao, D.; Wang, Y.-H.; Yan, B.; Xu, B.-Q. Manipulation of Pt∧Ag Nanostructures for Advanced Electrocatalyst. *J. Phys. Chem. C* **2009**, *113*, 1242−1250.

(73) Varshney, S.; Bar-Ziv, R.; Zidki, T. On the Remarkable Performance of Silver-based Alloy Nanoparticles in 4-Nitrophenol Catalytic Reduction. *ChemCatChem* **2020**, *12*, 4680−4688.

(74) Stephens, I. E. L.; Bondarenko, A. S.; Perez-Alonso, F. J.; Calle-Vallejo, F.; Bech, L.; Johansson, T. P.; Jepsen, A. K.; Frydendal, R.; Knudsen, B. P.; Rossmeisl, J.; Chorkendorff, I. Tuning the Activity of Pt(111) for Oxygen Electroreduction by Subsurface Alloying. *J. Am. Chem. Soc.* **2011**, *133*, 5485−5491.

(75) Merrill, N. A.; Nitka, T. T.; McKee, E. M.; Merino, K. C.; Drummy, L. F.; Lee, S.; Reinhart, B.; Ren, Y.; Munro, C. J.; Pylypenko, S.; Frenkel, A. I.; Bedford, N. M.; Knecht, M. R. Effects of Metal Composition and Ratio on Peptide-Templated Multimetallic PdPt Nanomaterials. *ACS Appl. Mater. Interfaces* **2017**, *9*, 8030−8040.

(76) Zhu, S.; Yue, J.; Qin, X.; Wei, Z.; Liang, Z.; Adzic, R. R.; Brankovic, S. R.; Du, Z.; Shao, M. The Role of Citric Acid in Perfecting Platinum Monolayer on Palladium Nanoparticles during the Surface Limited Redox Replacement Reaction. *J. Electrochem. Soc.* **2016**, *163*, D3040−D3046.

https://doi.org/10.1021/acs.chemmater.2c02659
Chem. Mater. 2022, 34, 9282−9293